ACS Energy LETTERS

http://pubs.acs.org/journal/aelccp

Tailoring Thick Film Crystallization and Facet Orientation via Potassium Acetate for Efficient Bifacial Perovskite Solar Cells

Xianggang Chen, Miao Yang, Xiaoxu Sun, Xing Li,* Yuhang Xie, Xuzheng Feng, Jixiang Tang, Longfei Yan, Shuyuan Fan, Songyuan Dai, Wenzhong Shen, and Molang Cai*

Cite This: ACS Energy Lett. 2025, 10, 3620−3628

Read Online

ACCESS | Metrics & More | Article Recommendations | Supporting Information

ABSTRACT: Bifacial perovskite solar cells (PSCs) require micron-thick perovskite layers to compensate for optical loss from transparent electrodes, but high defect densities limit efficiency. Here, we introduce a potassium acetate (KAc) post-treatment on microthick PbI_2 films to form an amorphous KAc-PbI_2 intermediate, which facilitates ammonium salt incorporation and promotes perovskite crystallization. During the second step, released Ac^- and K^+ ions selectively adsorb onto (111) and (001) facets, respectively, directing vertical crystal growth with (001) orientation. This strategy reduces defect density and improves film quality in thick perovskite layers. As a result, the bifacial PSC achieves a power conversion efficiency (PCE) of 21.33%, bifaciality exceeding 80%, and a record power generation density (PGD) of 24.72 mW cm^{-2} under 0.2 albedo, representing the highest reported PGD for n-i-p bifacial PSCs. After 500 h of continuous illumination at the maximum power point, the KAc-treated bifacial device retained its initial PCE.

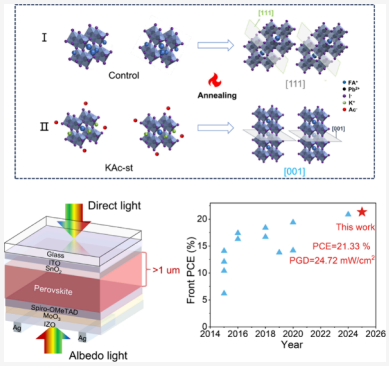

Perovskite solar cells (PSCs), which employ these materials as light-absorbing layers, have demonstrated remarkable progress, with power conversion efficiencies (PCEs) increasing from an initial value of 3.8% to a record high of 27%.[1,2] These advancements underscore the significant commercial potential of PSCs. To further enhance the power output per unit area, bifacial configurations capable of harnessing both direct and diffuse sunlight from both sides of the PSC have been explored.[3−7] Compared to conventional single-sided PSCs, bifacial devices utilize reflected sunlight from the environment on the rear side, thereby requiring thicker perovskite films to compensate for the light loss caused by transparent electrodes.[8] There exists a strong correlation between film thickness, light absorption, and device performance, with photocurrent density peaking at the micrometer scale.[9] Although increasing the perovskite layer thickness to the micron level enhances light harvesting and results in higher photocurrent density, it also introduces challenges such as unfavorable solubility of high-concentration precursor solutions and grain boundaries in both vertical and lateral directions.[10−12] These issues often lead to poor crystallization and increased defect density losses, thereby limiting efficiency and resulting in power outputs that only approach approximately 24 mW cm^{-2} under 0.2 albedo.[13]

The intermediate phase has been extensively investigated for its role in regulating the crystallization of perovskite films.[14−16] For example, the PbI_2(DMSO) and PbI_2-(DMSO)-MAI intermediate phases are formed through strong coordination interactions, which effectively retard the rapid reaction between FAI and PbI_2, thereby improving film quality.[17] However, the fabrication of thick perovskite films often necessitates high concentrations of PbI_2 and DMSO in the precursor solution, resulting in the aggregation of intermediate phases and consequently inferior film quality.[18,19] To date, limited strategies have been developed to address this challenge. The high viscosity of the MAAc ionic liquid enables a greater volume of precursor solution to remain during spin-coating at low concentrations, while a multistep annealing process facilitates uniform crystallization of thick films.[20] Halide rubidium additives have been demonstrated to enhance the solubility of intermediate phases and passivate defects in perovskite films.[13] Through a strain regulation strategy (SRS) based on layer-by-layer deposition to lock compressive strain, the PCE of thick-film devices was enhanced to 22.9%.[21] Recent

Received: May 26, 2025
Revised: June 21, 2025
Accepted: June 23, 2025

https://doi.org/10.1021/acsenergylett.5c01603
ACS Energy Lett. 2025, 10, 3620−3628

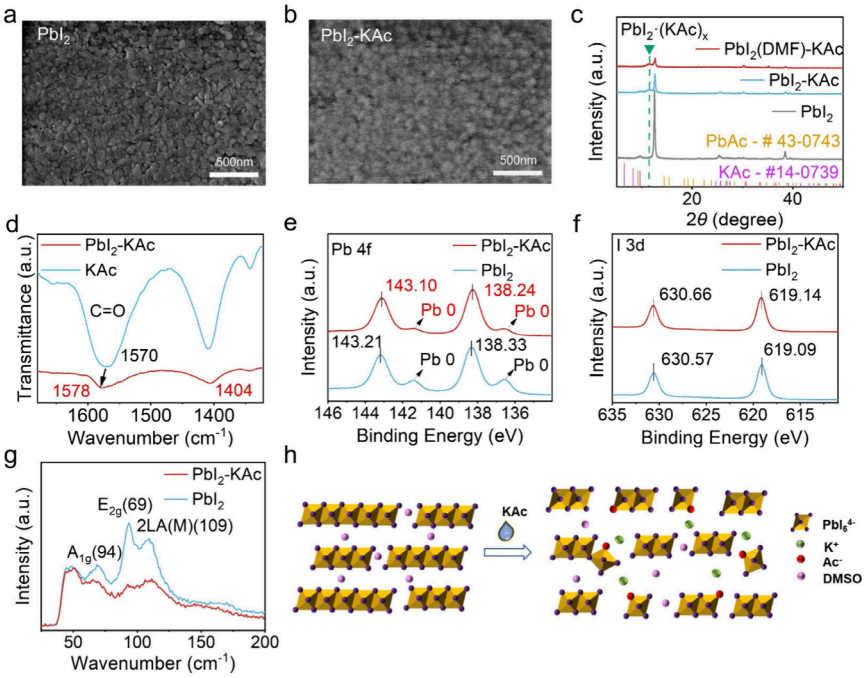

Figure 1. SEM top-view images of (a) PbI_2 and (b) PbI_2 -KAc film. (c) XRD of PbI_2 films and standard PDF cards for $Pb(Ac)_2$ and KAc. (d) FTIR spectra of KAc powder and PbI_2−KAc powder. (e-f) XPS of 4f and I 3d in PbI_2 and PbI_2 -KAc film. (g) Raman spectroscopy of PbI_2 film. (h) Schematic diagram of the mechanism of action of KAc solution treatment on PbI_2.

studies have indicated that coherent grain boundaries formed by high Miller index grains (e.g., (211) facets) and low Miller index grains (e.g., (001) facets) reduce defects and nonradiative recombination, enabling the preparation of high-quality micron-scale thick-film perovskites.[9] The fabricated p-i-n structured perovskite solar cells achieved an efficiency of 26.1% for small-area devices. Therefore, controlling the orientation of facets at grain boundaries represents an effective approach to minimize defects and improve the performance of microscale thick-film devices.

The (001) facet, well-known for its low defect density, facilitates a high photocurrent output.[22,23] In contrast, the (111) facet exhibits superior thermal, photonic, and moisture stability.[24,25] However, in micron-thick perovskite films, high defect concentrations may offset the optical advantages associated with increased thickness, even though structural stability is preserved. Therefore, guiding the formation of high-quality crystals with a specific (001) facet orientation emerges as a critical strategy to simultaneously enhance device performance, based on our understanding. In this study, we present a crystal facet engineering strategy based on potassium acetate (KAc) surface treatment (KAc-ST), which simultaneously addresses the issues of incomplete PbI_2 conversion and uncontrolled crystal orientation in thick perovskite films. The interaction between Ac^- and PbI_2 reduces the crystallinity of PbI_2, facilitating its complete conversion to perovskite. More importantly, the differential adsorption energies of K^+ and Ac^- on various α-$FAPbI_3$ crystal facets inhibit the growth of the (111) facet while preferentially promoting the formation of the (001) orientation, thereby reducing the generation of defect sites. This strategy, which controls defect density through the modulation of crystal facet orientation, not only significantly improves crystal quality, but also mitigates carrier recombination in thicker films. As a result, the resulting thick-film PSCs achieved an efficiency of 24.29%, while the bifacial PSCs demonstrated 21.33% efficiency with ≈80% bifaciality and 24.72 mW cm^{-2} power generation density (PGD) under an albedo of 0.2. This represents the highest PGD reported for n-i-p bifacial PSCs to date. After 500 h of continuous illumination at the maximum power point, the KAc-treated bifacial device retained its initial PCE.

The process for preparing perovskite films from PbI_2 films is shown in Figure S1. For convenience, we refer to the untreated PbI_2 films as "Control" and the PbI_2 films treated with KAc solution as "KAc-ST". We first investigated the effect of KAc solution surface treatment on the morphology of PbI_2 films. As shown in Figures 1a,b, the grain boundaries of PbI_2 films became blurred after KAc treatment, compared to the untreated films. The AFM morphology of PbI_2 films (Figure S2) exhibited a similar trend, with the surface roughness of the PbI_2 films decreasing after KAc treatment. These results suggest that PbI_2 films undergo a transition to an amorphous state upon treatment with KAc solution. Furthermore, we used X-ray diffraction (XRD) to study the effect of KAc treatment on the crystallinity of PbI_2 films (Figure S3). With the increase in KAc solution concentration, the crystallinity of PbI_2 gradually decreases. Notably, when the KAc concentration exceeds 2 mg/mL, a broad diffraction peak appears at 2θ = 11.4° accompanied by reduced crystallinity. To address the concern that the formation of the intermediate phase might be caused by the solvent itself, we treated PbI_2 films with pure isopropanol (IPA) without KAc (Figure S4). XRD analysis of the treated films showed no significant change in crystallinity compared to the untreated films. No peak shifts or new diffraction peaks were observed, thereby ruling out the possibility that the new peak originates from the solvent. To further investigate the nature of the intermediate phase, we directly synthesized it by reacting KAc with PbI_2 and performed XRD analysis on the resulting material (Figure S5). Interestingly, upon addition of KAc, the characteristic

https://doi.org/10.1021/acsenergylett.5c01603
ACS Energy Lett. 2025, 10, 3620−3628

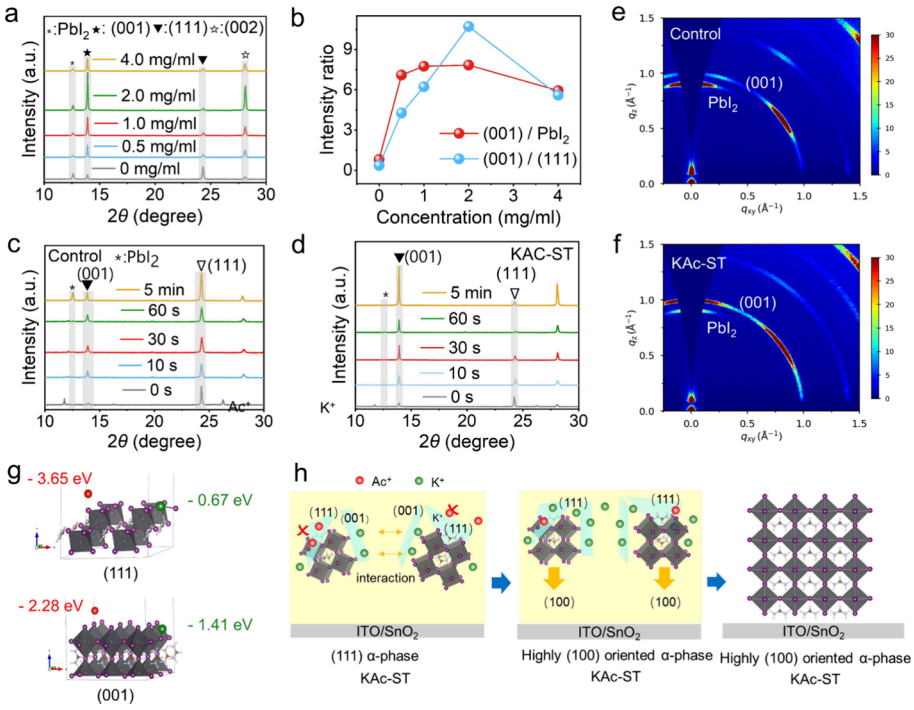

Figure 2. (a) XRD of perovskite films prepared with different concentrations of KAc solution. (b) The ratio of different diffraction peak intensities. XRD of (c) control and (d) KAc-ST perovskite films at different annealing times. GIWAXS of (e) control and (f) KAc-ST perovskite films. (g) Calculation model for adsorption energy of K^+ and Ac^-. (h) Schematic diagram of the mechanism for KAc-ST strategy to obtain (001) preferred crystal facet orientation.

PbI_2 diffraction peak at 2θ = 12.6° disappeared, and no new peaks were observed. Further comparison of the standard PDF cards for $Pb(Ac)_2$ (#43−0743) and KAc (#14−0739) with the XRD patterns reveals that the PbI_2 film treated with KAc-ST exhibits a new peak at 2θ = 11.4°, which is absent in pure $Pb(Ac)_2$ or KAc, indicating the formation of a new intermediate phase in the treated PbI_2 film, preliminarily identified as $PbI_2{\cdot}(KAc)_x$. To further explore the composition of this intermediate phase, PbI_2 films were prepared using pure DMF as the solvent and treated with KAc solution (to ensure solubility, the PbI_2 concentration was reduced to 0.5M). The XRD pattern (Figure 1c) also revealed a diffraction peak at 2θ = 11.4°, indicating that the intermediate phase resulted from the interaction between PbI_2 and KAc rather than the solvent (DMSO). Fourier transform infrared (FT-IR) spectra of the KAc-treated PbI_2 films and KAc powder (Figure 1d) revealed a shift in the C═O absorption peak from 1570 cm^{-1} (in KAc) to 1578 cm^{-1}, further confirming the interaction between Ac^- and PbI_2. X-ray photoelectron spectroscopy (XPS) analysis of Pb and I elements in PbI_2 films (Figures 1e,f) revealed that the binding energy of the Pb 4f core level decreased from 143.21 and 138.33 eV (untreated film) to 143.10 and 138.24 eV (KAc-treated film). In contrast, the binding energy of the I 3d core level increased slightly, from 630.57 and 619.09 eV to 630.66 and 619.14 eV. The greater change in Pb 4f binding energy suggests that the interaction between PbI_2 and KAc is primarily governed by Pb^{2+} and Ac^-. Typically, core-level binding energy decreases when an atom gains higher electron density. Ac^-, as an electron donor, forms coordination bonds with Pb^{2+}, reducing the Pb 4f binding energy. In addition, the XPS spectrum of the control perovskite exhibits significant Pb^0 signals, which arise from the decomposition of PbI_2 films under X-rays (Figure1 e). As nonradiative recombination centers, Pb^0 leads to the introduction of extra deep defect levels and a reduction in trap activation energy, thereby enhancing nonradiative recombination and accelerating perovskite degradation. In the KAc-treated films, the Pb^0 signals are suppressed, indicating that KAc effectively enhances the stability of PbI_2 films.

Raman spectroscopy (Figure 1 g) provided further evidence of this interaction. The characteristic peaks of PbI_2 at 69 cm^{-1} (E_{2g}), 94 cm^{-1} (A_{1g}), and 109 cm^{-1} (2LA(M)) were significantly suppressed after KAc treatment. These peaks correspond to shearing motion between iodine layers (E_{2g}) and symmetric stretching of Pb−I bonds (A_{1g}). Their suppression suggests that the one-dimensional layered structure of PbI_2 was disrupted, leading to reduced crystallinity. UV−vis absorption spectra (Figure S6) confirmed that the absorbance of PbI_2 films did not decrease after KAc treatment, excluding the possibility of partial PbI_2 removal during treatment. Based on the Raman and XPS results, a plausible interaction mechanism between KAc and PbI_2 is proposed (Figure 1h). Ac^- partially substitutes I^- in the lattice, forming coordination bonds with Pb^{2+} and disrupting the layered structure of PbI_2, thereby reducing its crystallinity. This interaction also weakens the bonding between I^- and Pb^{2+}, slightly increasing the binding energy of the I 3d core level. Meanwhile, K^+ ions are attracted to the periphery of the PbI_2-$(KAc)_x$ complex through electrostatic interactions, further increasing the spacing between iodine layers, consistent with the suppression of E_{2g} and A_{1g} peaks in Raman spectra.

To investigate the effects of KAc-ST on the crystallization of perovskite films after annealing, we characterized perovskite films coated on SnO_2 substrates. X-ray diffraction (XRD) results of perovskite films treated with different KAc concentrations are shown in Figure 2a. The control perovskite

https://doi.org/10.1021/acsenergylett.5c01603
ACS Energy Lett. 2025, 10, 3620−3628

film exhibited a strong signal at 2θ = 12.6°, corresponding to PbI_2, with an intensity even higher than that of the perovskite (001) facet at 2θ = 13.9°. This indicates incomplete PbI_2 conversion in conventional two-step perovskite films.[26] Furthermore, the diffraction peak of the (111) facet (2θ = 24.3°) in control films was stronger than that of the (001) facet, consistent with previous reports. In contrast, perovskite films prepared using the KAc-ST strategy exhibited significantly enhanced diffraction intensity for the (001) facet, with the (111) facet suppressed. Optimizing the KAc concentration to 2 mg/mL resulted in the highest intensity and smallest full width at half-maximum (fwhm) for the (001) peak (Figure S7), indicating superior crystal quality. The intensity ratios of (001)/PbI_2 and (001)/(111) were also maximized at this concentration (Figure 2b). The stacking orientation of crystal facets in perovskite films plays a crucial role in carrier transport.[27,28] Figure 2e,f display the grazing-incidence wide-angle X-ray scattering (GIWAXS) results for the perovskite films. The PbI_2 signal in the KAc-ST films was significantly reduced, consistent with conventional XRD results. Furthermore, the stacking orientation of the perovskite (001) facet shifted. In control films, the (001) facet was inclined toward the substrate, whereas in KAc-ST films, the stacking orientation of the (001) facet aligned perpendicular to the substrate. Integration of the GIWAXS signal in the vertical direction (85−95°) shows enhanced diffraction intensity of the (001) facet in the KAc-ST film compared to the control (Figure S8), indicating that the perovskite grows preferentially along the vertical direction.

To explore the potential mechanism behind the preferential (001) facet orientation observed in KAc-ST films, we conducted XRD measurements on PbI_2 films treated with LiAc, NaAc, and KAc, as shown in Figure S9. The results indicate that only KAc induces the formation of an intermediate phase. Furthermore, perovskite films fabricated from these alkali acetate-treated PbI_2 layers show that only the KAc-treated film exhibits a clear transformation in crystal facet orientation. We attribute this to the smaller ionic radii of Li^+ and Na^+, which may allow them to migrate into the bulk phase during surface treatment. Moreover, compared with K^+, Na^+ and Li^+ possess lower polarizability or electrostatic interaction strength due to their smaller ionic sizes or higher charge densities, which prevents them from forming intermediate phases that facilitate perovskite formation and thus fail to induce similar crystal orientation transformations. To further validate this mechanism, we fabricated perovskite films using a KI-treated PbI_2 precursor for comparison. XRD results (Figure S10) and the intensity ratio of (001)/(111) planes (Table S1) show that K^+ alone does not significantly enhance crystal orientation. This confirms the existence of a synergistic effect between K^+ and Ac^- in directing crystal facet formation. As shown in Figures 2c,d, both the control and KAc-ST perovskite films initially exhibit dominant (111) facets before annealing. Notably, the characteristic peak of the PbI_2−KAc intermediate phase at 2θ = 11.4° disappears (Figures 2d and S11). While the control film continues to grow along the (111) facet, the KAc-ST film transitions from (111) to (001) as the primary facet orientation. Importantly, no XRD peak shifts are observed for FA-based perovskites after annealing, indicating that K^+ and Ac^- do not incorporate into the final perovskite lattice, likely due to their ionic radii and incompatibility with the α-$FAPbI_3$ crystal structure. Based on these findings, we hypothesize that the transition in facet orientation is driven by differences in the adsorption energies of K^+ and Ac^- on different crystal facets. During crystal growth, preferential adsorption due to annealing suppresses growth along the (111) facet and promotes growth along the (001) facet.

To investigate the role of K^+ and Ac^- in determining the crystal growth orientation, we first performed density functional theory (DFT) calculations to evaluate the adsorption energy (Eads) of Ac^- on the (001) and (111) surfaces of α-$FAPbI_3$, as shown in Figure 2g. The adsorption energy of Ac^- on the (111) surface was 3.65 eV, significantly higher than that on the (001) surface (2.28 eV), indicating preferential adsorption on the (111) facet. This selective adsorption stabilizes the (111) facet and kinetically retards its growth, thereby promoting crystal growth along the (001) direction, which is consistent with the XRD results of the KAc-ST-treated perovskite. During crystal growth, K^+ ions are present on the crystal surface and grain boundaries. Moreover, we calculated the adsorption energies of K^+ on the (001) and (111) surfaces of α-$FAPbI_3$, Figure 2g. K^+ ions showed stronger adsorption on the (001) surface, with an Eads of 1.41 eV, compared to 0.67 eV on the (111) surface, indicating a higher affinity for the (001) facet. Electrostatic repulsion between adjacent K^+ ions suppresses lateral grain coalescence, effectively inhibiting horizontal growth. According to the top-down nucleation mechanism, these effects synergistically promote vertical growth while suppressing disordered lateral crystallization (Figure 2h). This transformation is consistent with the GIWAXS results, which reveal enhanced vertical stacking (Figure 2e,f). Ultimately, during annealing, the small ionic radius of K^+ prevents its incorporation into the α-$FAPbI_3$ lattice, allowing it to be replaced by FA^+, thereby improving crystal packing. Cross-sectional SEM images further demonstrate that, compared to the control film, the KAc-ST-treated perovskite film exhibits vertically aligned grains, which may result from the change in crystal orientation (Figure S12). Therefore, the preferential adsorption of K^+ and Ac^- alters the facet orientation of the perovskite crystals. This ultimately drives vertical growth along the (001) plane, significantly reducing defect density and enhancing device performance.

Furthermore, we directly introduced KAc into the PbI_2 precursor to investigate whether a similar effect could be achieved. To explore this, composite films were prepared by incorporating KAc into the PbI_2 precursor solution (denoted as the KAc additive). SEM analysis of the PbI_2 films revealed that the KAc additive film (Figure S13a) retained distinguishable crystalline grains but exhibited surface voids, which may facilitate subsequent reaction with ammonium salts. However, XRD analysis confirmed the absence of new diffraction peaks at 2θ = 11.4°, in contrast to the KAc-ST PbI_2 films (Figure S13c). This suggests that the homogeneous dispersion of K^+/Ac^- ions in the bulk phase may inhibit the formation of the intermediate phase ($PbI_2 \cdot (KAc)_x$). XRD and SEM characterization of the corresponding perovskite films showed reduced residual PbI_2 on the surface of the KAc additive films (Figure S13b,d). However, no apparent crystal facet transformation or preferential orientation was observed (Figure S13d). Although bulk doping with KAc additives moderately reduces the crystallinity of PbI_2, the uniform ion distribution results in random facet evolution and leaves residual unreacted PbI_2 on the surface. Therefore, although both methods reduce the crystallinity of PbI_2, only the KAc-ST method can precisely control the crystal orientation of the resulting perovskite. This differs from the mechanisms reported in previous literature.[29]

https://doi.org/10.1021/acsenergylett.5c01603
ACS Energy Lett. 2025, 10, 3620−3628

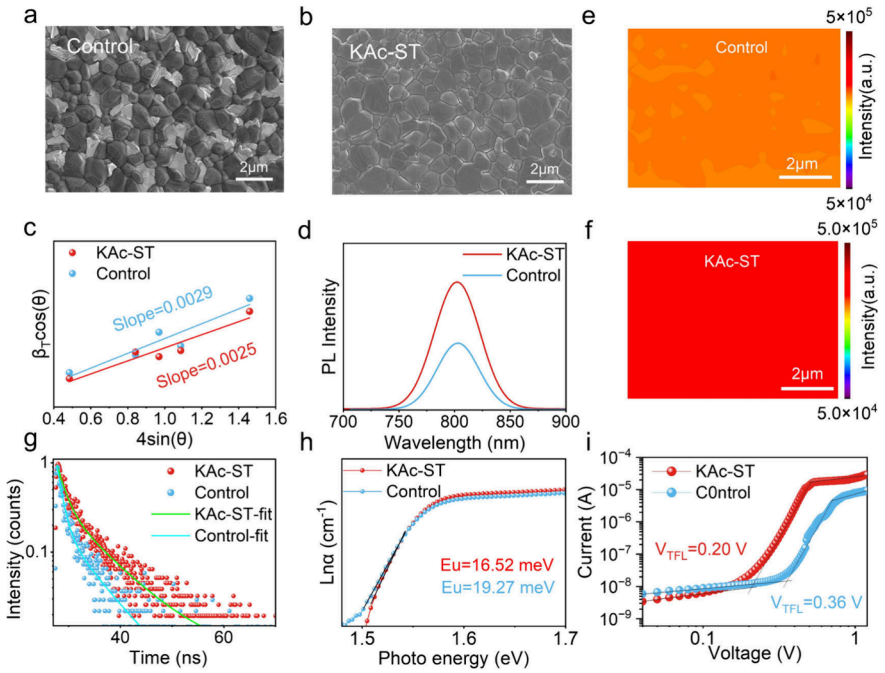

Figure 3. SEM top-view images of (a) Control and (b) KAc-ST perovskite films. (c) W−H plots of the control and KAc-ST perovskite films. (d) PL of the control and KAc-ST perovskite films deposited on a glass substrate. PL mapping of (e) the control and (f) KAc-ST perovskite films. (g) TRPL of the control and KAc-ST perovskite films deposited on a glass substrate. (h) Logarithm of absorption coefficient versus photo energy of the perovskite films without and with KAc-ST. (i) The space-charge-limited current versus voltage curves of the device with the control and KAc-ST perovskite films.

Based on these findings, we selected the surface treatment strategy for further investigation.

To investigate the universality of the KAc-ST strategy in thick films, we further examined perovskite films with a thickness of 1500 nm. As shown in Figure S14a, the untreated film exhibits abundant white, flaky PbI_2 residues on the surface, which become more prominent with increased thickness. This is attributed to the limited diffusion and reactivity of the ammonium salt (FAI), making it difficult to fully convert the thick PbI_2 layer into perovskite. Upon applying the KAc-ST treatment, SEM images (Figure S14b,d) reveal a significant reduction in surface PbI_2 residues and improved grain connectivity in the cross-section. In comparison, the treated films display reduced PbI_2 signals and a dominant (001) orientation (Figure S15), consistent with the crystal orientation evolution observed in 1 μm-thick films (Figure 2a). A perovskite thickness of approximately 1 μm is sufficient to meet the light absorption requirements for bifacial solar cells. Therefore, considering both optical absorption efficiency and film quality, our study focuses on further investigation of micron-thick perovskite films.

Previous studies have reported significant differences in grain morphology between $FAPbI_3$ perovskite films with (001) and (111) crystal facet orientations. Perovskite single crystals with different facet orientations exhibit distinct grain structures.[27] Based on the SEM top-view morphology of perovskite films (Figure 3a,b), the KAc-ST strategy effectively altered the grain morphology. The control perovskite films showed pyramid-like grains, likely due to the dominant (111) facet orientation. In contrast, the KAc-ST films exhibited flatter grains as the crystal facet orientation shifted from (111) to (001). Statistical analysis of grain sizes in the regions shown in Figure S16 revealed an increase in average grain size from 0.87 μm (control films) to 1.00 μm (KAc-ST films). The enlarged grains reduced the number of grain boundaries, which are typically associated with defects such as dislocations, impurity defects, and vacancies.[30,31] Thus, larger grains help to minimize defects in perovskite films.

As shown in Figures S17a,b, we supplemented the film morphology by AFM with the root-mean-square roughness (Rq) decreasing from 39.92 to 31.56 nm, favoring better contact between the perovskite layer and the HTL layer, thereby reducing carrier recombination at the interface. The Kelvin probe force microscopy (KPFM) can measure the contact potential difference (CPD) between the tip and the sample surface, and the CPD can be used to obtain the work function information on the sample surface. As shown, the CPD of the Control film is −0.148 V, significantly lower than that of the KAc-ST film (0.106 V). The increase in CPD means a decrease in the work function of the sample surface under the same test conditions. Figures S17c,d show that the KAc-ST strategy increases the average CPD value of the perovskite film, indicating that the surface W_F of the perovskite film decreases, which is consistent with the conclusion reported that the (001) crystal facet has a lower work function.[32] Reducing the W_F of the perovskite film is beneficial to improving the open-circuit voltage (V_{oc}) of the device. The residual lattice strain in mixed halide perovskite films was calculated using the Williamson-Hall (W−H) method from XRD spectra[33] (Figure 3c; see Supplementary Note 1 for details). The residual strain, determined from the slope of the fitted line, decreased from 0.0029 in control films to 0.0025 in KAc-ST films. This strain release helps to mitigate defect formation associated with lattice expansion stress. Steady-state and time-resolved photoluminescence (PL and TRPL) spectra of perovskite/Glass films corroborated these observations. The KAc-ST perovskite films exhibited significantly enhanced PL intensity (Figure 3d), and PL mapping images (Figure 4b)

https://doi.org/10.1021/acsenergylett.5c01603
ACS Energy Lett. 2025, 10, 3620−3628

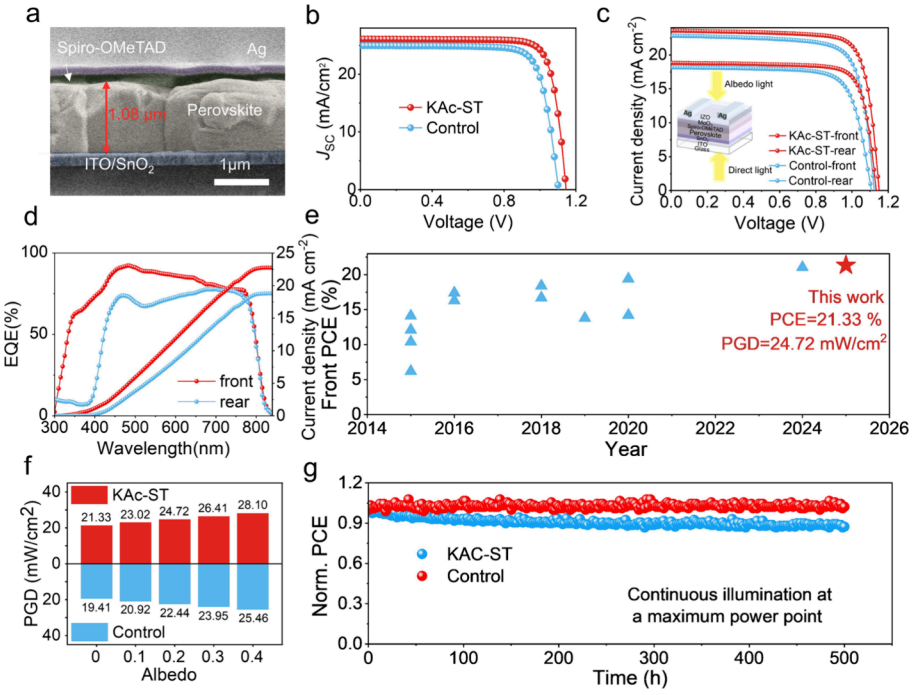

Figure 4. (a) SEM of the thick film device. (b) $J-V$ curve of the champion thick film device. (c) $J-V$ curve of the champion bifacial PSC device, the inset is a schematic diagram of the structure of a bifacial PSC. (d) EQE and integrated current of the bifacial PSC device. (e) Statistical diagram of the efficiency and PGD of formal structure bifacial PSCs. (f) Statistical charts of the most effective rates and PGD of control and KAc-ST device. (g) Bifacial PSC device stability of unencapsulated devices stored at 25 °C and ∼25% RH under continuous 1 Sun illumination in air.

further confirmed the improvements in peak intensity and uniformity. The carrier lifetime of KAc-ST films was longer (Figure 3g and Table S3), indicating reduced nonradiative recombination losses.[18,34] The reduced losses can be attributed to the lower defect density in the (001) facets and the larger grain sizes. We plotted the logarithmic absorption coefficient (α) as a function of photon energy to study the Urbach energy (Eu) (Figure 3h). It is well-known that a lower Eu reflects higher structural quality of the perovskite film and reduced energetic disorder. In this study, Eu was calculated from the UV−vis absorption spectra of the perovskite films (Figure S17) using the relation $\alpha = \alpha_0 \cdot \exp(h\nu/\mathrm{Eu})$, where α is the absorption coefficient, α_0 is a constant, h is Planck's constant, and ν is the frequency of light (with $h\nu$ representing the photon energy).[35] The Eu value decreased from 16.52 to 19.27 meV, indicating that the band tail states are reduced by the KAc-ST, which may help minimize the V_{oc} deficit. UV−vis absorption spectra (Figure S18) revealed no significant changes in the spectral absorption range of KAc-ST perovskite films compared to control films. However, in the 550−800 nm wavelength range, the KAc-ST films exhibited enhanced absorbance at constant film thickness. This improvement can be attributed to reduced PbI_2 residues and enhanced perovskite crystallinity, promoting increased absorption of effective wavelengths and enhancing photocurrent density. We fabricated pure electron devices with an ITO/SnO_2/perovskite/C_{60}/Au structure to quantify defect density using the space-charge-limited current (SCLC) method. The trap-filled limit voltage (V_{TFL}) was proportional to the defect state density (N_t).[36] Control devices showed a V_{TFL} of 0.36 V (Figure 3h), which decreased to 0.20 V in KAc-ST devices (Figure 3i). Correspondingly, the N_t value decreased from 8.26 × 10^{15} cm^{-3} to 3.25 × 10^{15} cm^{-3}.

To systematically evaluate the impact of the KAc-ST strategy on the device performance of micron-scale perovskite films (thickness ∼ 1 μm, SEM cross-section shown in Figure 4a), we constructed a n-i-p-type perovskite solar cell with the structure of glass/ITO/SnO_2/perovskite/Spiro-OMeTAD/Ag. The $J-V$ testing under AM 1.5G standard solar illumination (100 mW cm^{-2}) demonstrated a significant performance improvement for devices based on the KAc-ST strategy (Figure 4b). The optimized device achieved a V_{oc} of 1.15 V, a J_{sc} of 26.09 mA cm^{-2}, a FF of 80.97%, and a PCE of 24.29% (Table S4), demonstrating a significant increase compared to the control device (PCE = 21.64%). This represents one of the highest efficiencies reported for perovskite devices fabricated with micron-thick films to date (Table S7). As shown in Figure 4d, the external quantum efficiency (EQE) spectra of devices with and without the KAc-ST strategy exhibit integrated current densities of 25.05 and 24.18 mA cm^{-2}, respectively, demonstrating a mismatch of less than 5% compared to the J_{sc} values obtained from $J-V$ curves (Figure S19). Figure 4c depicts the schematic diagram of the bifacial PSC prepared for our study, with the device structure being ITO/SnO_2/perovskite/Spiro-OMeTAD/MoO_3/IZO/Ag. To ensure efficient light capture on both sides of the bifacial PSC, we used a thicker perovskite film with KAc-ST. As a result, the average visible light transmittance of our FA-based perovskite device in the wavelength range of 400−850 nm is only 4.9% (Figure S20), which is significantly lower than the reported semitransparent perovskite solar cells (ST-PSC) used in tandem configurations.[37] We compared the performance of perovskite devices with the KAc-ST strategy to that of the control devices without modification. Figure 4d shows the best PCE for the control and KAc-ST strategies, with the conversion efficiency for glass-side incident light reaching 21.33%, V_{oc} of 1.14 V, J_{sc}

https://doi.org/10.1021/acsenergylett.5c01603
ACS Energy Lett. 2025, 10, 3620−3628

of 23.44 mA cm^{-2}, and 79.67%. For electrode-side incident light, the conversion efficiency is 16.93%, with V_{oc} of 1.13 V, J_{sc} of 18.83 mA cm^{-2}, and FF of 79.59% (Tables S5 and S6). The PGD of KAc-ST exceeds 24.72 mW/cm^2 (Figure 4f), which is the highest record achieved by n-i-p bifacial PSCs (Figure 4e). Table S8 summarizes the research achievements of formal structured bifacial perovskite solar cells in recent years. This indicates a significant improvement in the performance of the devices fabricated using the KAc-ST strategy. The EQE measurements were performed on the devices (Figure 4d), showing higher quantum efficiency in the visible light range for devices treated with KAc-ST. This improvement is partially attributed to the increased light absorption difference due to the larger grain size, as well as the impact of defect-induced nonradiative recombination on carrier transport within the device. Figure 4d shows the integration of EQE over the 300−850 nm wavelength range, resulting in front and back current densities of 22.75 and 18.69 mA cm^{-2}, respectively, which closely match the $J-V$ test results (Figure S21). The decrease in J_{sc} of approximately 20% is mainly attributed to parasitic absorption in the Spiro-OMeTAD layer, as there is considerable parasitic absorption between the front and back electrodes.[38] To evaluate the efficiency gain under bifacial illumination, under one sun illumination, the simulated PGDs of bifacial KAc-ST devices are 23.02, 24.72, 26.41, and 28.10 mW cm^{-2} respectively, and the albedos are 0.1, 0.2, 0.3, and 0.4 respectively. For control (Figure 4f), the device performance is significantly improved. To better understand the physical reasons behind the device performance improvement, a comparison of dark-state $J-V$ curves shows a significant reduction in the saturation current density for the KAc-ST devices, further confirming the reduction in trap density (Figure S22). Furthermore, electrochemical impedance spectroscopy (EIS) in dark was used to assess carrier transport and recombination behavior.[39] In the Nyquist plot, semicircles of varying sizes are observed over different frequency ranges. The charge recombination resistance (R_{rec}) at the interface is determined by the low-frequency region. The fitted R_{rec} values are shown in Figure S23. Based on the equivalent circuit model (Figure S24), the R_{rec} value of the bifacial perovskite film (1683 Ω) is higher than the R_{rec} value of the control perovskite device (1288 Ω) (Figure S23). The higher recombination resistance contributes to enhanced photovoltaic performance of the bifacial perovskite films by effectively separating charges in the corresponding collection layers. To further investigate the intrinsic transport mechanisms of the control and KAc-ST devices, a Mott−Schottky (M-S) analysis was performed using capacitance−voltage ($C-V$) measurements to directly describe the built-in potential (V_{bi}) of the devices (Figure S25). In the linear M-S plot, the KAc-ST device shows the largest slope, with the V_{bi} value of the control device being 0.84 V, and the V_{bi} value of the KAc-ST device being 0.88 V. The enhanced V_{bi} indicates an increase in the internal driving force for carrier transport to the device's energy, which also contributes to improved photovoltaic performance. Additionally, we plotted the relationship between V_{oc} and light intensity (Figure S26). The slope for the control device is 1.63 K_BT/q, while the slope for the bifacial device is much smaller (1.43 K_BT/q), where K_B is the Boltzmann constant, T is the temperature, and q is the charge.[40] Previous studies have shown that deviations from the slope of K_BT/q reflect defect recombination in the device. This result confirms that harmful defect recombination in the perovskite layer has been significantly alleviated, thereby reasonably improving the device performance. Further aging tests were conducted on the bifacial PSC. As shown in Figure S24, the KAc-ST-based packaged devices demonstrated excellent stability under continuous sunlight exposure in a nitrogen glovebox at 40 ± 5 °C, with no significant degradation observed even after 1000 h (Figure S27). In contrast, the PCE of the control group dropped to 60% of their initial efficiency (Figure S28, Table S7) after 1000 h. To evaluate the effectiveness of the KAc-ST strategy under ambient conditions, we conducted maximum power point (MPP) tracking tests on unencapsulated bifacial PSCs under continuous 1 Sun (100 mW/cm^2) illumination in air. After 500 h, the KAc-ST devices maintained nearly unchanged power conversion efficiency, while the control devices degraded to below 90% of their initial efficiency (Figure 4g). The improvement in light stability can be attributed to the modification of the perovskite film morphology and crystallinity by KAc-ST, as well as the reduction in both bulk and surface defects in the perovskite.

This study presents the KAc-ST strategy, where surface treatment of PbI_2 films with KAc solution disrupts the one-dimensional structure of PbI_2 through the interaction between Ac- and Pb^{2+}. The presence of K^+ expands the interlayer spacing, forming the PbI_2-$(KAc)_x$ intermediate phase, which reduces PbI_2 crystallinity and promotes a more complete conversion to perovskite while improving crystallinity. DFT calculations show that Ac^- preferentially adsorbs on the (111) surface, inhibiting growth along the (111) direction. K^+ ions preferentially adsorb at the crystal surface and grain boundaries during the growth process. Moreover, K^+ exhibits a stronger affinity for the (001) facet, as indicated by its higher adsorption energy compared to the (111) facet. The electrostatic repulsion between adjacent K^+ ions effectively inhibits lateral grain merging, thereby suppressing horizontal growth and promoting vertical crystallization along the (001) direction. This results in perovskite films with (001)-preferred orientation. This leads to perovskite films with a vertically aligned (001) orientation. These improvements enhance light absorption, produce smoother film morphology, and reduce defect density. Using a KAC-st strategy, the thick-film PSC achieved an efficiency of 24.29%. The fabricated bifacial PSC reached 21.33% efficiency, exhibiting ≈80% bifaciality and 24.72 mW cm^{-2} PGD under an albedo of 0.2. After 500 h of continuous illumination at the maximum power point, the KAc-treated bifacial device retained its initial PCE. This study provides a foundation for improving the efficiency and stability of bifacial PSCs.

■ ASSOCIATED CONTENT

Supporting Information

The Supporting Information is available free of charge at https://pubs.acs.org/doi/10.1021/acsenergylett.5c01603.

Experimental details covering materials, perovskite thin film fabrication, device fabrication, and characterization. Schematic diagram in Figure S1. AFM top-view images in Figures S2 and S17. XRD spectra in Figures S3−S5, S8−S11, S13, and S15. UV−vis absorption spectra in Figures S6 and S18. Diffraction peak intensity and fwhm in Figure S7. Cross-sectional SEM images in Figures S12 and S14. Grain size statistics in Figure S16. SEM top-view images in Figures S13 and S14. EQE curves in Figures S19 and S21. Transmittance spectrum in Figure

https://doi.org/10.1021/acsenergylett.5c01603
ACS Energy Lett. 2025, 10, 3620−3628

S20. Dark $J-V$ curves in Figure S22. EIS curves (including Nyquist plot fitting) in Figure S23. Mott–Schottky plot in Figure S25. V_{oc} dependence on light intensity in Figure S26. Unencapsulated device stability tracking in Figure S27. $J-V$ curve in Figure S28. Diffraction peak intensity ratio in Table S1. Calculation results and TRPL in Tables S2 and S3. Detailed $J-V$ scan parameters in Tables S4–S7. Device characteristics summaries in Tables S8 and S9 (PDF)

AUTHOR INFORMATION

Corresponding Authors

Xing Li − *Institute of Microelectronics of Chinese Academy of Sciences, Beijing 100029, P. R. China;* orcid.org/0000-0002-0794-3613; Email: lixing2021@ime.ac.cn

Molang Cai − *School of New Energy and Beijing Key Laboratory of Novel Thin-Film Solar Cells, North China Electric Power University, Beijing 102206, P. R. China;* orcid.org/0000-0001-8568-6897; Email: molangcai@ncepu.edu.cn

Authors

Xianggang Chen − *School of New Energy and Beijing Key Laboratory of Novel Thin-Film Solar Cells, North China Electric Power University, Beijing 102206, P. R. China*

Miao Yang − *School of New Energy and Beijing Key Laboratory of Novel Thin-Film Solar Cells, North China Electric Power University, Beijing 102206, P. R. China*

Xiaoxu Sun − *School of New Energy and Beijing Key Laboratory of Novel Thin-Film Solar Cells, North China Electric Power University, Beijing 102206, P. R. China*

Yuhang Xie − *School of New Energy and Beijing Key Laboratory of Novel Thin-Film Solar Cells, North China Electric Power University, Beijing 102206, P. R. China*

Xuzheng Feng − *School of New Energy and Beijing Key Laboratory of Novel Thin-Film Solar Cells, North China Electric Power University, Beijing 102206, P. R. China*

Jixiang Tang − *School of New Energy, North China Electric Power University, Beijing 102206, P. R. China; Institute of Microelectronics of Chinese Academy of Sciences, Beijing 100029, P. R. China*

Longfei Yan − *School of New Energy and Beijing Key Laboratory of Novel Thin-Film Solar Cells, North China Electric Power University, Beijing 102206, P. R. China*

Shuyuan Fan − *School of New Energy and Beijing Key Laboratory of Novel Thin-Film Solar Cells, North China Electric Power University, Beijing 102206, P. R. China*

Songyuan Dai − *School of New Energy and Beijing Key Laboratory of Novel Thin-Film Solar Cells, North China Electric Power University, Beijing 102206, P. R. China;* orcid.org/0000-0001-5710-9208

Wenzhong Shen − *Institute of Solar Energy, Key Laboratory of Artificial Structures and Quantum Control (Ministry of Education), School of Physics and Astronomy, Shanghai Jiao Tong University, Shanghai 200240, China;* orcid.org/0000-0003-4527-9183

Complete contact information is available at: https://pubs.acs.org/10.1021/acsenergylett.5c01603

Author Contributions

X.L., M.C.: Designed and directed the study. M.Y., X.C.: Fabricated and characterized the perovskite samples and devices. J.X.T., X.S., M.Y., X.C.: Conducted stability measurements of perovskite devices. X.C.: Wrote the manuscript. All of the authors commented on the manuscript.

Notes

The authors declare no competing financial interest.

ACKNOWLEDGMENTS

This work was sponsored by the National Natural Science Foundation of China (52202169 and 12175305), the Beijing Nova Program (20230484298), the Special Foundation for Carbon Peak Carbon Neutralization Technology Innovation Program Jiangsu Province (BE2022026), and the Shanghai New Energy Technology Research and Development Project China (No.24DZ3000900).

REFERENCES

(1) Solar Cell Efficiency chart, efficiency chart-27, 2025. https://www.nrel.gov/pv/cell-efficiency.html (accessed 14–05–2025).

(2) Kojima, A.; Teshima, K.; Shirai, Y.; Miyasaka, T. Organometal Halide Perovskites as Visible-Light Sensitizers for Photovoltaic Cells. *J. Am. Chem. Soc.* **2009**, *131* (17), 6050–6051.

(3) Wu, H.; Cheng, Y.; Ma, J.; Zhang, J.; Zhang, Y.; Song, Y.; Peng, S. Pivotal Routes for Maximizing Semitransparent Perovskite Solar Cell Performance: Photon Propagation Management and Carrier Kinetics Regulation. *Adv. Mater.* **2023**, *35* (5), No. 2206574.

(4) Chen, X.; Yuan, Z.; Fan, S.; Feng, X.; Sun, X.; Tang, J.; Yan, L.; Wang, Z.; Li, Z.; Cui, X.; Zhang, Z.; Chen, J.; Dai, S.; Cai, M.; et al. Enhanced Light Transmittance of Electron Transport Layer through Bilayer SnO_2 for High-Performance Semitransparent Perovskite Solar Cells. *ChemSusChem* **2025**, *18* (11), No. e202402582.

(5) Jiang, Q.; Song, Z.; Bramante, R. C.; Ndione, P. F.; Tirawat, R.; Berry, J. J.; Yan, Y.; Zhu, K. Highly efficient bifacial single-junction perovskite solar cells. *Joule* **2023**, *7* (7), 1543–1555.

(6) Cui, X.; Li, X.; Wang, Z.; Li, Z.; Chen, X.; Tang, J.; Feng, X.; La, S.; Chen, J.; Zhang, Z.; et al. MoO_3/Au/Ag/MoO_3 multilayer transparent electrode enables high light utilization of semitransparent perovskite solar cells. *Device* **2025**, *3* (1), No. 100558.

(7) Yang, Y.; Hoang, M. T.; Chiu, W.-H.; Yu, Y.; Wang, H. Efficient Bifacial Semitransparent Perovskite Solar Cells Using Down-Conversion 2D Perovskite Nanoplatelets–Poly(Methyl Methacrylate) Composite Film. *Small Struct.* **2024**, *5* (6), No. 2300547.

(8) Luo, X.; Gao, Y.; Zhu, P.; Han, Q.; Lin, R.; Gao, H.; Wang, Y.; Zhu, J.; Li, S.; Tan, H. Record Photocurrent Density over 26 mA cm^{-2} in Planar Perovskite Solar Cells Enabled by Antireflective Cascaded Electron Transport Layer. *Sol. RRL* **2020**, *4* (7), No. 2000169.

(9) Li, S.; Xiao, Y.; Su, R.; Xu, W.; Luo, D.; Huang, P.; Dai, L.; Chen, P.; Caprioglio, P.; Elmestekawy, K. A.; et al. Coherent growth of high-Miller-index facets enhances perovskite solar cells. *Nature* **2024**, *635* (8040), 874–881.

(10) Wang, Y.; Akel, S.; Klingebiel, B.; Kirchartz, T. Hole Transporting Bilayers for Efficient Micrometer-Thick Perovskite Solar Cells. *Adv. Energy Mater.* **2024**, *14* (5), No. 2302614.

(11) Chen, B.; Baek, S.-W.; Hou, Y.; Aydin, E.; De Bastiani, M.; Scheffel, B.; Proppe, A.; Huang, Z.; Wei, M.; Wang, Y.-K.; et al. Enhanced optical path and electron diffusion length enable high-efficiency perovskite tandems. *Nat. Commun.* **2020**, *11* (1), 1257.

(12) Yang, G.; Ni, Z.; Yu, Z. J.; Larson, B. W.; Yu, Z.; Chen, B.; Alasfour, A.; Xiao, X.; Luther, J. M.; Holman, Z. C.; et al. Defect engineering in wide-bandgap perovskites for efficient perovskite–silicon tandem solar cells. *Nat. Photonics* **2022**, *16* (8), 588–594.

(13) Chen, J.; Sun, X.; Wang, Z.; Cui, X.; Chen, X.; Li, Z.; Feng, X.; Tang, J.; Yang, M.; Yuan, Z.; et al. Rubidium Halide Additive Engineering for Efficient and Stable Bifacial Perovskite Solar Cells. *Adv. Funct. Mater.* **2025**, *35* (3), No. 2411010.

(14) Xiang, W.; Zhang, J.; Liu, S.; Albrecht, S.; Hagfeldt, A.; Wang, Z. Intermediate phase engineering of halide perovskites for photovoltaics. *Joule* **2022**, *6* (2), 315−339.
(15) Shao, W.; Wang, H.; Ye, F.; Wang, C.; Wang, C.; Cui, H.; Dong, K.; Ge, Y.; Wang, T.; Ke, W.; et al. Modulation of nucleation and crystallization in PbI2 films promoting preferential perovskite orientation growth for efficient solar cells. *Energy Environ. Sci.* **2023**, *16* (1), 252−264.
(16) Tong, G.; Son, D.-Y.; Ono, L. K.; Liu, Y.; Hu, Y.; Zhang, H.; Jamshaid, A.; Qiu, L.; Liu, Z.; Qi, Y. Scalable Fabrication of >90 cm^2 Perovskite Solar Modules with >1000 h Operational Stability Based on the Intermediate Phase Strategy. *Adv. Energy Mater.* **2021**, *11* (10), No. 2003712.
(17) Jung, M.; Ji, S.-G.; Kim, G.; Seok, S. I. Perovskite precursor solution chemistry: from fundamentals to photovoltaic applications. *Chem. Soc. Rev.* **2019**, *48* (7), 2011−2038.
(18) Chen, J.; Sun, X.; Wang, Z.; Cui, X.; Chen, X.; Li, Z.; Feng, X.; Tang, J.; Yang, M.; Yuan, Z.; et al. Rubidium Halide Additive Engineering for Efficient and Stable Bifacial Perovskite Solar Cells. *Adv. Funct. Mater.* **2025**, *35* (3), No. 2411010.
(19) Mo, K.; Zhu, X.; Yang, M.; Xue, Z.; Li, S.; li, M.; Yang, Y.; Cheng, S.; Li, H.; Lin, Q.; et al. Minimizing DMSO Residues in Perovskite Films for Efficient and Long-Term Stable Solar Cells. *Adv. Energy Mater.* **2025**, *15* (19), No. 2404538.
(20) Hu, J.-F.; Chen, G.; Yu, S.-Z.; Lin, Y.-X.; Wang, K.-Y.; Li, Z.-W.; Zhang, G.-D.; Pan, T.-F.; Li, Y.-J.; Li, M.-J.; et al. Efficient micrometer-scale thick-film perovskite solar cells with superior stability. *Rare Met.* **2024**, *43* (4), 1647−1657.
(21) Shi, P.; Xu, J.; Yavuz, I.; Huang, T.; Tan, S.; Zhao, K.; Zhang, X.; Tian, Y.; Wang, S.; Fan, W.; et al. Strain regulates the photovoltaic performance of thick-film perovskites. *Nat. Commun.* **2024**, *15* (1), 2579.
(22) Zheng, G.; Zhu, C.; Ma, J.; Zhang, X.; Tang, G.; Li, R.; Chen, Y.; Li, L.; Hu, J.; Hong, J.; et al. Manipulation of facet orientation in hybrid perovskite polycrystalline films by cation cascade. *Nat. Commun.* **2018**, *9* (1), 2793.
(23) Zhu, C.; Wang, C.; Zhang, P.; Ma, S.; Chen, Y.; Zhang, Y.; Yang, N.; Xiao, M.; Cheng, X.; Gao, Z.; et al. Topochemical assembly minimizes lattice heterogeneity in polycrystalline halide perovskites. *Joule* **2023**, *7* (10), 2361−2375.
(24) Qu, S.; Huang, H.; Wang, J.; Cui, P.; Li, Y.; Wang, M.; Li, L.; Yang, F.; Sun, C.; Zhang, Q.; et al. Revealing and Inhibiting the Facet-related Ion Migration for Efficient and Stable Perovskite Solar Cells. *Angew. Chem., Int. Ed.* **2025**, *64* (4), No. e202415949.
(25) Li, D.; Sun, X.; Zhang, Y.; Guan, Z.; Yue, Y.; Wang, Q.; Zhao, L.; Liu, F.; Wei, J.; Li, H. Uniaxial-Oriented Perovskite Films with Controllable Orientation. *Adv. Sci.* **2024**, *11* (19), No. 2401184.
(26) Jiang, Q.; Zhao, Y.; Zhang, X.; Yang, X.; Chen, Y.; Chu, Z.; Ye, Q.; Li, X.; Yin, Z.; You, J. Surface passivation of perovskite film for efficient solar cells. *Nat. Photonics* **2019**, *13* (7), 460−466.
(27) Ma, C.; Kang, M.-C.; Lee, S.-H.; Kwon, S. J.; Cha, H.-W.; Yang, C.-W.; Park, N.-G. Photovoltaically top-performing perovskite crystal facets. *Joule* **2022**, *6* (11), 2626−2643.
(28) Luo, C.; Zheng, G.; Gao, F.; Wang, X.; Zhao, Y.; Gao, X.; Zhao, Q. Facet orientation tailoring via 2D-seed- induced growth enables highly efficient and stable perovskite solar cells. *Joule* **2022**, *6* (1), 240−257.
(29) Yang, Y.; Liang, J.; Zhang, Z.; Tian, C.; Wu, X.; Zheng, Y.; Huang, Y.; Wang, J.; Zhou, Z.; He, M.; et al. Suppressing Residual Lead Iodide and Defects in Sequential-Deposited Perovskite Solar Cell via Bidentate Potassium Dichloroacetate Ligand. *ChemSusChem* **2022**, *15* (6), No. e202102474.
(30) Shao, Y.; Fang, Y.; Li, T.; Wang, Q.; Dong, Q.; Deng, Y.; Yuan, Y.; Wei, H.; Wang, M.; Gruverman, A.; et al. Grain boundary dominated ion migration in polycrystalline organic−inorganic halide perovskite films. *Energy Environ. Sci.* **2016**, *9* (5), 1752−1759.
(31) Dymshits, A.; Henning, A.; Segev, G.; Rosenwaks, Y.; Etgar, L. The electronic structure of metal oxide/organo metal halide perovskite junctions in perovskite based solar cells. *Sci. Rep.* **2015**, *5* (1), 8704.
(32) Wang, R.; Xue, J.; Wang, K.-L.; Wang, Z.-K.; Luo, Y.; Fenning, D.; Xu, G.; Nuryyeva, S.; Huang, T.; Zhao, Y.; et al. Constructive molecular configurations for surface-defect passivation of perovskite photovoltaics. *Science* **2019**, *366* (6472), 1509−1513.
(33) Chen, X.; Peng, H.; Sun, X.; Yan, L.; Feng, X.; Fan, S.; Jia, R.; Dai, S.; Li, X.; Zhang, X.; et al. The Mixed Phases of α and γ-$CsPbI_3$ Enable Efficient and Stable Semitransparent Solar Cells. *Small* **2025**, *21* (14), No. e2500710.
(34) Hang, P.; Xie, J.; Kan, C.; Li, B.; Zhang, Y.; Gao, P.; Yang, D.; Yu, X. Stabilizing Fullerene for Burn-in-Free and Stable Perovskite Solar Cells under Ultraviolet Preconditioning and Light Soaking. *Adv. Mater.* **2021**, *33* (10), No. 2006910.
(35) Kim, G.; Min, H.; Lee, K. S.; Lee, D. Y.; Yoon, S. M.; Seok, S. I. Impact of strain relaxation on performance of α-formamidinium lead iodide perovskite solar cells. *Science* **2020**, *370* (6512), 108−112.
(36) Ma, X.; Pan, J.; Wang, Y.; Gao, X.; Hu, M.; Ku, Z.; Ma, Y.; Huang, F.; Cheng, Y.-B.; Lu, J. Bromide complimented methylammonium-free wide bandgap perovskite solar modules with high efficiency and stability. *Chem. Eng. J.* **2022**, *445*, No. 136626.
(37) Naqvi, S. D. H.; Son, K.; Jung, W.; Hwang, H. u.; Lee, S.; Lee, A.; Keum, M.; Kim, S.; Kim, J. W.; Kang, M. G.; et al. Mitigating Intrinsic Interfacial Degradation in Semi-Transparent Perovskite Solar Cells for High Efficiency and Long-Term Stability. *Adv. Energy Mater.* **2023**, *13* (47), No. 2302147.
(38) Jäger, K.; Korte, L.; Rech, B.; Albrecht, S. Numerical optical optimization of monolithic planar perovskite-silicon tandem solar cells with regular and inverted device architectures. *Opt. Express* **2017**, *25* (12), A473−A482.
(39) Shi, P.; Ding, Y.; Ren, Y.; Shi, X.; Arain, Z.; Liu, C.; Liu, X.; Cai, M.; Cao, G.; Nazeeruddin, M. K.; et al. Template-Assisted Formation of High-Quality α-Phase $HC(NH_2)_2PbI_3$ Perovskite Solar Cells. *Adv. Sci.* **2019**, *6* (21), No. 1901591.
(40) Li, Z.; Li, X.; Chen, X.; Cui, X.; Guo, C.; Feng, X.; Ren, D.; Mo, Y.; Yang, M.; Huang, H.; et al. In situ epitaxial growth of blocking structure in mixed-halide wide-band-gap perovskites for efficient photovoltaics. *Joule* **2023**, *7* (6), 1363−1381.

https://doi.org/10.1021/acsenergylett.5c01603
ACS Energy Lett. 2025, 10, 3620−3628